https://doi.org/10.1016/j.atmosenv.2021.118540

Ozone and its precursors in a high-elevation and highly forested region in central China: origins, in-situ photochemistry and implications of regional transport

X. Lyu[1], H. Guo[1*], W. Zhang[2], H. Cheng[2], D. Yao[1], H. Lu[1], L. Zhang[1], Y. Zeren[1], X. Liu[1], Z. Qian[1], S. Wang[1,†]

[1] Department of Civil and Environmental Engineering, The Hong Kong Polytechnic University, Hong Kong, China

[2] School of Resource and Environmental Sciences, Wuhan University, Wuhan, China

[†] Now at Environmental Microbiology Laboratory, École polytechnique fédérale de Lausanne, Lausanne, Switzerland

* Corresponding author: Hai Guo (hai.guo@polyu.edu.hk)

Abstract: Atmospheric chemistry observation and modelling in alpine areas have strong indication of regional air quality. In this study, one-month continuous ozone (O_3) measurement at a high-elevation and highly forested site in central China, in combination with observations at similar stations, indicated elevated O_3 levels in the free troposphere (FT) over China. Uninterrupted O_3 injuries to the old-growth forest in the study region were expected. FT O_3 overwhelmed daytime photochemical formation at the site, and the transport of O_3 from the north (e.g., Guanzhong Plain) was most significant. Air masses from the adjacent southwest and south regions (*e.g.*, Chongqing) contained higher levels of nitric oxide, sulfur dioxide, fine particles and volatile organic compounds (VOCs) in association with vehicular and industrial emissions. In contrast, air masses from the northeast (*e.g.*, North China Plain) were laden with combustion tracers. The in-situ photochemistry modelling confirmed weak O_3 formation at the site. For the reasons, the insufficient nitrogen oxides suppressed transformation of peroxyl radicals to alkoxy and hydroxyl radicals, resulting in considerable losses of peroxyl radicals via self-reactions. VOCs showed little impact on in-situ O_3 production, and accounted for net consumption of OH, with isoprene as the most predominant OH depleting species. This study fills the gaps in observation of O_3 and its precursors and modelling of in-situ photochemistry in high-elevation regions of central China, and provides hints for the impacts of transport on air pollution in this region.

Keywords: Ozone; Volatile organic compounds; In-situ photochemistry; High-elevation station; Background site

1. Introduction

Tropospheric ozone (O_3), as a greenhouse gas, exaggerates global warming effect (Fishman et al., 1979). It also plays important roles in atmospheric chemistry by acting as an oxidant and a source of hydroxyl radical (Atkinson and Aschmann, 1993). High levels of O_3 harm human health and vegetation (Reich and Amundson, 1985; Lippmann, 1991). Tropospheric O_3 is formed through reactions between volatile organic compounds (VOC) and nitrogen oxides (NO_x) in the presence of sunlight (Atkinson, 2000), with intrusion of stratospheric O_3 as an additional source (Hocking et al., 2007). The increasing anthropogenic emissions and post–2013 reductions in NO_x and fine particulate matter ($PM_{2.5}$) concentrations have led to rising levels of tropospheric O_3 across China in past decades (Sun et al., 2016; Wang et al., 2017; Li et al., 2019a, Liu and Wang, 2020).

O_3 levels at high-elevation stations with sparse anthropogenic emissions are essential indicator of regional to hemispheric O_3 pollution. Study on four decades' O_3 variations at Mauna Loa (MLO, 3397 m a.s.l.) uncovered the modulations of El Niño–Southern Oscillation and Pacific–North American pattern on cross-Pacific transport of Eurasian emissions (Lin et al., 2014). Surface observations in and near the Alps indicated the leveling-off of O_3 since 2000, driven by the balancing effect of emission reductions in Europe and North America and increasing hemispheric background O_3 (Cui et al., 2011; Logan et al., 2012). The increase of autumnal O_3 over Qinghai-Tibet Plateau, China during 1994–2013 was found to be mainly attributed to transport from South and Southeast Asia (Xu et al., 2018). A global chemistry–climate model identified rising emissions in the NCP as the primary factor leading to increase of summertime O_3 during 2003–2015 at Mt. Tai (1534 m a.s.l.), the highest mountain in the NCP (Sun et al., 2016).

A handful of studies highlighted O_3 pollution in central China (Lu et al., 2017; Zeng et al., 2018). However, the characteristics of air pollutants, their sources and/or O_3 photochemistry were seldom investigated in regional background atmosphere. As far as O_3 is concerned, there was no ground-based observations or ozonesonde measurements at high-elevation stations. Recently, Lei et al. (2021) conducted a related study at a mountainous site in a rural area. However, the site was merely 750 m a.s.l. and it was not far enough away from big cities, *e.g.,* ~100 km to Wuhan (the capital of Hubei province). In this study, we for the first time present 1-month data of O_3 and other criteria air pollutants at Shennongjia (SNJ), the highest mountain in central China (3106 m a.s.l.). VOCs were collected on 9 days, consisting of 67 daytime samples and 12 nighttime samples. The nighttime O_3, which most likely represented O_3 in the FT, were compared with those at some other high-elevation stations in the Northern Hemisphere. The dependences of concentrations and compositions of air pollutants on air mass origins are discussed. In-situ O_3 photochemistry is studied with an observation–based photochemical box model.

2. Methods

2.1. Continuous measurement, Sample collection and Chemical analysis

Continuous measurements of O_3 and other criteria air pollutants were conducted at the SNJ National Station for Background Atmospheric Monitoring (NSBAM) (110.271° E, 31.456° N,

2950 m a.s.l.) throughout September 2019, as shown in Figure 1. The site was in the middle of four city clusters, i.e. Guanzhong Plain (GP) to the north, NCP to the northeast, Yangtze Plain, Middle and Lower (YPML) to the east and Sichuan Basin (SB) to the southwest, and located in the largest old-growth forest in central China with the forest coverage rate of ~70%. Table S1 lists the instruments, detection limits and time resolutions for the measurements. The sampling inlets were 1–2 m above the rooftop of a 4-story building. 5-point calibrations were conducted to all the instruments before the sampling campaign, and daily zero checks were automatically performed. The original data were converted to and reported as hourly averages. It has been well documented that nitrogen dioxide (NO_2) measurement with chemiluminescence technique and molybdenum catalysis overestimates the real NO_2, due to conversion of oxidized nitrogen species to NO (Dunlea et al., 2007; Xu et al., 2013). The measured nitrogen dioxide, referred to as NO_2* hereinafter, should be used with caution. The CO data dropped by ~8% between 23:00 and 0:00 every day caused by the daily zero calibrations, and returned to normal at ~9:00. In view of the comparable magnitudes of drops among the days, we still use the data in this study. A mini weather station was deployed on the rooftop to monitor the meteorological parameters.

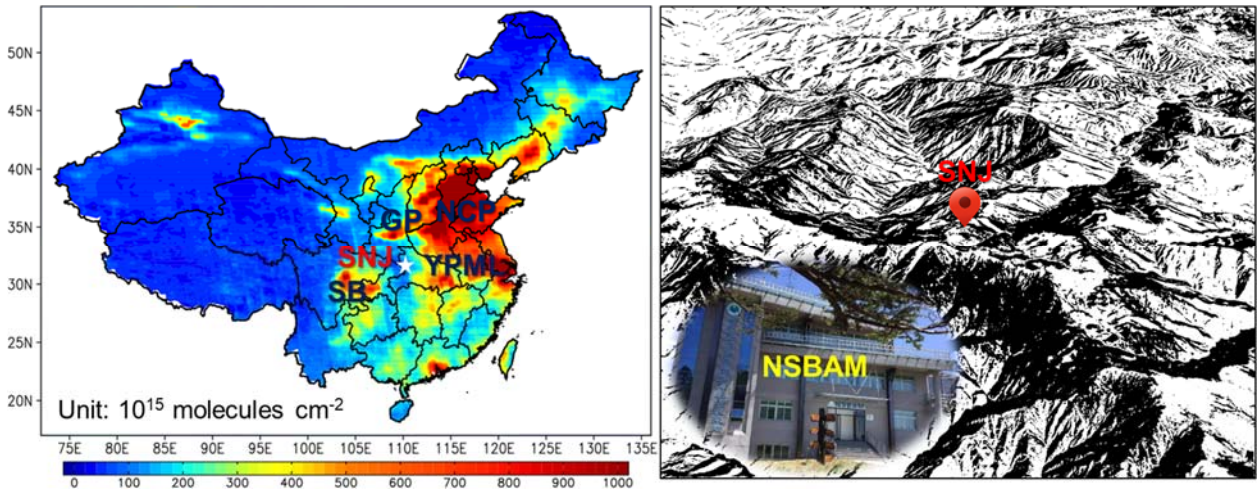

Figure 1. Location of the sampling site (left) and the nearby terrain (right). Background map in the left panel shows the mean column concentrations of NO_2 (a proxy of anthropogenic emissions) in 2019 (TEMIS-OMI data). The insert photo on the right panel is the NSBAM at SNJ.

1-hour VOC samples were collected using the pre-cleaned 2 L stainless steel canisters. The oxygenated VOCs (OVOCs) were trapped with silica cartridges coated with 2,4-dinitrophenylhydrazine (DNPH) for 2 hours per sample. Disposable O_3 scrubbers were connected in front of the DNPH cartridges to reduce O_3 interferences. In total, we obtained 79 and 60 samples of VOCs and OVOCs, respectively. The sampling scheme is shown in Table S2. While all the other samples were collected at the NSBAM, 16 VOC samples were collected on the road to the NSBAM at lower elevations, which are not used in this study.

The samples were shipped back to the laboratory for chemical analysis within 1 month. VOCs were analyzed using gas chromatography system with mass selective detection, flame ionization detection and electron capture detection. A high–performance liquid chromatography was used to

analyze OVOCs. The analysis procedures and quality control were described elsewhere (Lyu et al., 2019).

2.2. Model simulations

2.2.1. Backward trajectory analysis

The HYSPLIT model (v4.9) was utilized to simulate the trajectories of air masses reaching the site. The trajectory calculation was performed every 1 hour, lasting for 72 hours backwards. The calculations started at the NSBAM, with the initial height of 1965 m above ground level (a.g.l.). The height was determined based on the requirement that the simulated pressure at the starting point was close to the real pressure monitored at the site (mean: 715 hPa). Mountains tend to get smoothed out in HYSPLIT modelling which uses gridded meteorological data, leading to failure of reproducing the real heights of mountains (https://www.arl.noaa.gov/hysplit/hysplit-frequently-asked-questions-faqs/which-value-should-i-input-as-the-start-height/). Pressure is a good alternative to be referenced to. In this study, the mean simulated pressure was 909 hPa with the height of 100 m a.g.l., which meant that the model actually ran at a starting point ~2155 m below the sampling site. Through tests, we adopted the height of 1965 m a.g.l., with which the mean simulated pressure at the starting point was 729 hPa (~2% higher than the real pressure).

Figure 2 shows the ensemble of hourly trajectories in the whole month. 4 types of air masses were identified according to their origins, *i.e.*, short trajectories from the southwest and south (SWS), long trajectories from the south (S), trajectories from the northeast (NE) and those from the north (N). While the SWS, NE and N trajectories originated from or passed by the city cluster of SB, NCP and GP shown in Figure 1, respectively, very few trajectories were associated with YPML. The S trajectories were mainly originated from South China Sea (SCS). On the 9 VOC-sampling days, the trajectories were composed of SWS (Case I, 39.4%), NE (Case II, 19.9%) and S (Case III, 40.7%).

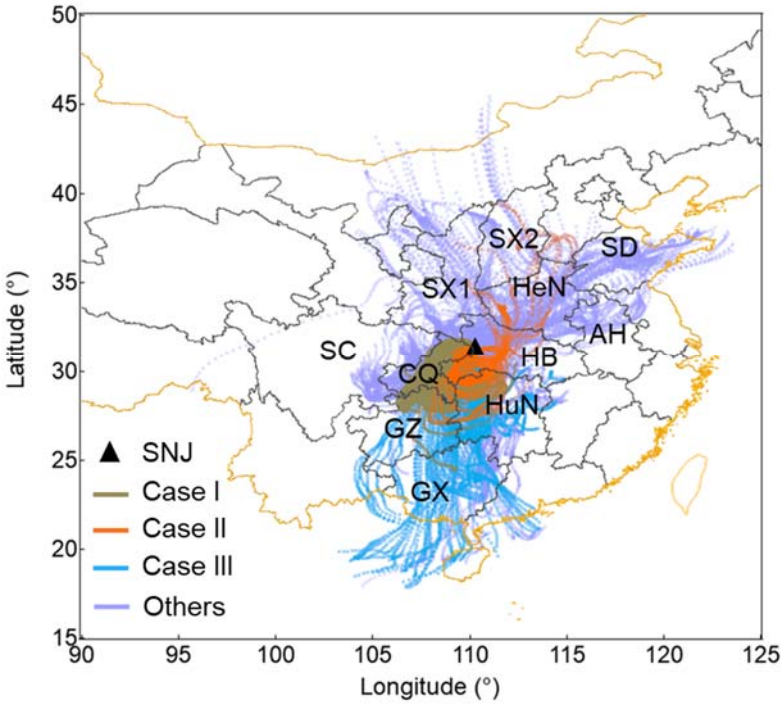

Figure 2. Ensemble of 72-hr backward trajectories at hourly resolution. AH: Anhui, CQ: Chongqing, GX: Guangxi, GZ: Guizhou, HB: Hubei, HeN: Henan, HuN: Hunan, SC: Sichuan, SD: Shandong, SX1: Shaanxi, SX2: Shanxi.

2.2.2. Modelling of in-situ photochemistry

An observation-based box model incorporating Master Chemical Mechanism (v3.2) was applied to understand the in-situ photochemistry. Details about the model have been elaborated in previous publications (Lyu et al., 2017a, 2019). The observed concentrations of air pollutants and values of meteorology, including 65 VOCs, 3 OVOCs (formaldehyde, acetaldehyde and acetone), sulfur dioxide (SO_2), carbon monoxide (CO), nitric oxide (NO), O_3, temperature and relative humidity were used to constrain the model. Specifically, the model read the observed values every 200 seconds. Limited by sampling resolutions, the input data were treated as constants within 1 hour and 2 hours for VOCs and OVOCs, respectively. Hourly data of VOCs were obtained using linear interpolations. For the days when nighttime samples were not collected, the average diurnal cycles for individual species were applied to the daytime samples to estimate the missing values at night. The field observation did not cover peroxyacetyl nitrate and nitrous acid, which complied with photochemical equilibriums in the model. While temperature and relative humidity were assigned as parameters, all the air pollutants were defined as variables, which meant that their concentrations could evolve over time. The photolysis rates of O_3 and NO_2 were calculated by a Tropospheric Ultraviolet and Visible (TUV) radiation model constrained by the observed solar radiations, following the method described previously (Lyu et al., 2019). All the simulations had a spin-up of 120 hours to stabilize the radicals and secondary species which were not input (e.g., OH and NO_2). For those of our interest, such as air pollutants, radicals or reaction pathways, the concentrations

or reaction rates were integrated and output at the resolution of 200 seconds, which were converted to hourly averages.

The measured NO_2* was not input to constrain the model. Instead, the model simulated NO_2 based on photochemical equilibrium by taking the sources (e.g., oxidation of NO by O_3 and peroxy radicals) and sinks (e.g., photolysis and reaction with OH) into account. Taking O_3, NO, NO_2 and isoprene (a representative of reactive VOCs) as examples, we compared their mixing ratios in model outputs with the observed values during 7:00–17:00 when photochemical reactions were relatively intensive (Figure S1). The mixing ratios of O_3 and isoprene were perfectly constrained to the observations. NO mixing ratios output from the model were ~36% lower than the observed values, due to the quick titration by O_3. Because of the positive bias in NO_2 measurement, it was reasonable that the simulated NO_2 was generally lower than NO_2*. However, it was over-predicted to exceed NO_2* in the morning and afternoon of 9 & 15 September, when the solar radiations were very weak (<100 W m^{-2}). This was caused by the inefficient photolysis of NO_2 and lack of dispersion (an inherent drawback of box model). The consequent effects on NO_2 simulation were amplified by reading the observed mixing ratios of NO and O_3 every 200 seconds. In spite of the uncertainties, we adopted the simulated NO_2 rather than the observed NO_2* in in-situ photochemistry modelling, due to the potentially large overestimates of NO_2*. The impacts of model inputs on the simulation results can be inferred from the sensitivity analysis in section 3.3.

3. Results

3.1. Concentrations and diurnal patterns

Figure 3(a) shows the average mixing ratios of O_3 at SNJ and other mountainous stations during 22:00–6:00 in the Northern Hemisphere. The averages of all hourly data, sampling details and data sources are provided in Table S3. Due to the high elevations of all the stations, the downhill winds most likely brought FT air to the sites at night (Lin et al., 2014). Thus, the averages during 22:00–6:00 when the O_3 levels were high and stable are treated as proxies of FT O_3. The time period was slightly different from that (0:00–8:00) adopted by Lin et al. (2014) at MLO, in order to reconcile the calculation periods at all the stations. It should be kept in mind that the FT O_3 levels are influenced by the abundances of O_3 precursors in the boundary layer and strength of stratosphere-troposphere exchange (Hegglin et al., 2015). At comparable elevations (~3,000 m), SNJ in central China (CC) had much higher O_3 than the stations in Europe (EU). The levels of FT O_3 over the NCP, southern China (SC) and eastern China (EC) were 1.5–2.2 times that over the western United States (WUS) at the elevation of 1,500–1,800 m, with the highest value observed at Mt. Tai. O_3 at WLG in western China also overwhelmed those over EU, WUS and North Pacific (NP). Overall, the comparisons demonstrated high FT O_3 over China, particularly in the NCP. The FT O_3 levels at SNJ in central China were only second to those at Mt. Tai in the NCP, bearing the different elevations in mind. The patterns remained unchanged, when the averages were calculated with whole day data (Table S3). Moreover, the dominance of O_3 at Mt. Tai over other stations was even more pronounced, due to the intensive O_3 formation in daytime there (Sun et al., 2016).

At SNJ, the threshold of O_3 causing forest damage (hourly average of 40 ppbv) was exceeded at the rate of 98.2%, by taking the 8:00–20:00 data into account. The Accumulated Ozone exposure over a Threshold of 40 ppbv (AOT40) was 34,050 ppbv·h during April–September, as calculated following the formula in Geernaert and Zlatev (2004) and under the assumption of no O_3 seasonality throughout this period. The AOT40 was most likely underestimated, as O_3 got the highest values in summer in central China. Despite this, the AOT40 was 3.4 times of 10,000 ppbv·h, a critical level corresponding to 5% loss of forest yield (WHO, 2000).

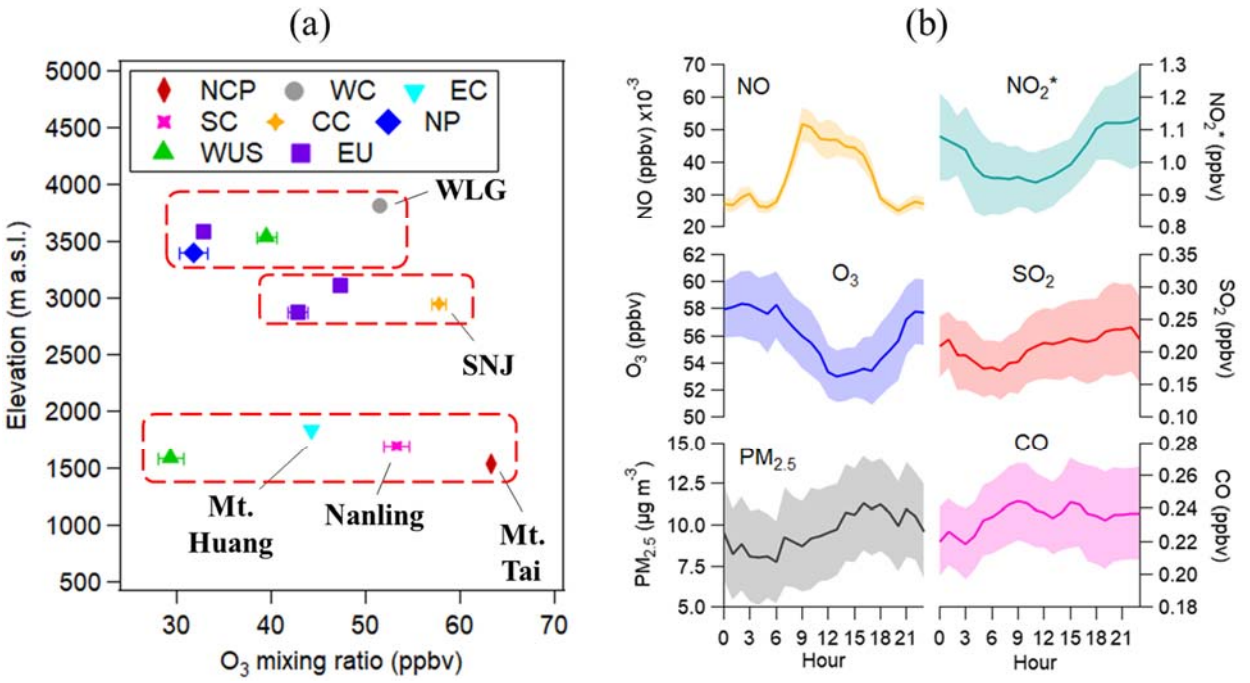

Figure 3. (a) Average O_3 mixing ratio against elevation at high-elevation and/or forested stations in the Northern Hemisphere. Inside the red boxes are stations at comparable elevations. (b) Average diurnal patterns of trace gases and $PM_{2.5}$ at SNJ in the whole September. Error bars and shaded areas represent 95% confidence intervals (C.I.s).

The diurnal patterns of O_3 and other criteria air pollutants at SNJ are shown in Figure 3(b). The higher levels of O_3 at night than in daytime were in line with those at many other high-elevation stations (Lin et al., 2014; Xu et al., 2016). As aforementioned, FT air laden with O_3 intruded at night via downhill winds. Conversely, the uphill winds brought boundary layer (BL) air with relatively low O_3 to the site in daytime. The phenomenon of lower BL O_3 than FT O_3 is common in remote regions but is not necessarily universal, especially in areas where anthropogenic emissions cause efficient O_3 production within BL (*e.g.*, Mt. Tai). The intrusion of BL air also led to the increases of $PM_{2.5}$ and SO_2 since the early morning and might partially contribute to the daytime NO, which increased at the same time as $PM_{2.5}$ and SO_2 and presented a broad peak in daytime. In addition to transport via uphill winds, NO_2 photolysis and variation of O_3 levels also played key roles in shaping the diurnal pattern of NO (Xue et al., 2011). For example, the sharp decrease in NO mixing ratio at ~15:00 was most likely due to the enhanced titration by O_3 and weakened photolysis of NO_2. The diurnal cycle of measured NO_2* was opposite to that of NO.

However, it could not be explained by photochemical equilibrium, due to the gaps in magnitudes of their changes, *i.e*., the large increment of NO_2* (~200 pptv) versus NO reduction of merely ~20 pptv from noon to evening. Instead, the resembling of NO_2* cycle to that of O_3 indicated the dominance of oxidized nitrogen species in NO_2*, which were formed as byproducts in O_3 formation. The diurnal variation of CO was not obvious, except for the drop (~8%) at 0:00 and recovery between 0:00 and ~9:00 caused by zero calibrations as mentioned in section 2.1. The relatively stable levels symbolized comparable mixing ratios of CO in FT and BL in this region.

Furthermore, Table 1 shows the average mixing ratios (or concentrations) of air pollutants and mean values of meteorological parameters in 4 types of air masses. O_3 and NO_2* mixing ratios were highest in type-N air masses, though the differences from those in other types were small and even insignificant. The lowest temperature and weak solar radiation implied that the higher levels of O_3 and NO_2* in type-N air were mainly attributable to photochemical processes in source regions (*i.e.,* GP) or during transport, instead of local formation. NO, SO_2 and $PM_{2.5}$, which were more associated with primary emissions, were most abundant in type-SWS air masses, indicating the transport of these air pollutants from Chongqing and the northern part of Hunan and Guizhou provinces. CO had the highest mixing ratios in type-NE air masses, in line with the enrichments of other combustion tracers identified from VOC measurements (*e.g*., ethane, ethyne, benzene and methyl chloride, see section 3.2). This demonstrated the higher intensities of combustion activities, such as biomass burning, in the NCP. The type-S air contained relatively low levels of air pollutants. On one hand, most of the air masses originated from SCS, where anthropogenic emissions were sparse. On the other hand, the average wind speed was the highest with the arrival of type-S air, which favored dispersion. In contrast, the other 3 types of air masses were more stagnant, based on the much lower wind speeds.

To sum up, O_3 and oxidized nitrogen species (inferred from the patterns of NO_2*) in the FT overwhelmed their daytime photochemical productions, and the transport was somewhat more significant from the north. BL development led to increases of NO, SO_2 and $PM_{2.5}$, which were most enhanced in air masses from the southwest and south adjacently. Bearing the measurement uncertainties in mind, we found no obvious difference between the FT and BL CO, but it had the highest mixing ratios in air masses from the northeast.

Table 1. Mixing ratios (or concentrations) of air pollutants and meteorology with 95% C.I.s in 4 types of air masses. Bolded fonts are the highest values.

Species/Parameter	SWS (*n* = 214)	S (*n* = 183)	NE (*n* = 224)	N (*n* = 99)
O_3 (ppbv)	56.5 ± 1.0	55.5 ± 1.0	54.9 ± 1.0	**57.2 ± 0.7**
NO (pptv)	**39.5 ± 2.0**	34.4 ± 1.4	32.7 ± 1.7	32.1 ± 2.0
NO_2* (ppbv)	1.07 ± 0.04	0.88 ± 0.03	1.06 ± 0.05	**1.08 ± 0.05**
SO_2 (ppbv)	**0.29 ± 0.03**	0.14 ± 0.01	0.18 ± 0.01	0.20 ± 0.02
CO (ppbv)	234 ± 6.5	231 ± 10.2	**255 ± 9.9**	214 ± 9.2
$PM_{2.5}$ (μg m^{-3})	**14.3 ± 1.1**	5.7 ± 0.9	8.4 ± 1.0	9.0 ± 0.9
Temperature (°C)	9.6 ± 0.3	**10.2 ± 0.3**	7.7 ± 0.6	4.0 ± 0.4
Relative Humidity (%)	87 ± 1.5	**96 ± 1.1**	84 ± 3.6	93 ± 1.7

Wind Speed (m s^{-1})	2.3 ± 0.2	**4.3 ± 0.3**	2.2 ± 0.3	2.4 ± 0.5
Solar Radiation (W m^{-2})	**189 ± 41**	77 ± 18	137 ± 49	109 ± 36
Pressure (hPa)	716 ± 0.4	717 ± 0.3	718 ± 0.5	**719 ± 0.4**
BL height (m) *	354 ± 59	295 ± 45	346 ± 62	**433 ± 96**

* BL height is derived from the ERA5 reanalysis dataset of European Centre for Medium-Range Weather Forecasts and is calculated with whole-day data.

3.2. Characteristics of VOCs

Measurements of VOCs in high-elevation regions were even scarcer than O_3 observations. The average mixing ratios of individual VOC and OVOC species at SNJ are listed in Table S4. Isoprene was the most abundant VOC at SNJ (2.24±0.53 ppbv), due to the emissions from old-growth forest. Only second to isoprene was acetone, followed by ethane, *i*-pentane, cyclopentane, methyl chloride (CH_3Cl) and ethyne, indicating the potential impacts of diverse sources including combustion, vehicular emissions and industrial processes (Liu et al., 2008).

Figure S2 compares the mixing ratios and compositions of VOCs at several mountainous stations in China. VOCs were collected in 3 types of air masses at SNJ and are discussed in 3 cases in this section, *i.e.*, Case I, II and III belonging to the type of SWS, NE and S, respectively. 29 VOCs, which were measured at all the stations, were focused. The total mixing ratios was highest at Tai Mo Shan (TMS) in Hong Kong, and lowest at WLG. Distance to sources was an important factor leading to the difference, as the altitude of WLG is ~6 times that of TMS. Besides, the Qinghai-Tibet Plateau where WLG located had much fewer emissions than Hong Kong. Despite that the sampling site had a higher altitude in this study, the mixing ratios of VOCs exceeded those at Mt. Tai in the NCP. This was partially due to the great abundances of biogenic VOCs (isoprene, α-pinene and β-pinene) at SNJ. When excluding these species, the total mixing ratios of VOCs in Case III at SNJ were ~12.5% lower than those at Mt. Tai. However, air masses in Case I and Case II still contained elevated levels of VOCs, with the mixing ratios ~10.4% and ~6.5% higher than those at Mt. Tai, respectively. In contrast to the impacts of aforementioned sources on VOCs at SNJ, combustion activities likely dominated the sources of VOCs at Mt. Tai, due to the high levels of ethane, ethyne, benzene and ethene (Liu et al., 2008; Zhu et al., 2017), while the dominance of toluene, propane and *n*/*i*-butanes at TMS signified large influence of vehicular emissions, especially emissions from vehicles fueled by liquefied petroleum gas (Lyu et al., 2017a,b).

Furthermore, we compared the VOC mixing ratios among the 3 types of air masses, as shown in Figure 4. OVOCs and biogenic VOCs are not included, due to the low detection rates and strong local emissions, respectively. Case I air masses were characterized by highest mixing ratios for VOCs related to gasoline vehicle emissions, such as *n*-butane, *n*/*i*-pentanes, 2-methylpentane and toluene. Cyclopentane and trichloroethylene also presented with greatest abundances in Case I, indicative of industrial emissions (Liu et al., 2008). In contrast, the Case II air masses were laden with low carbon number alkanes (ethane, propane and *i*-butane), ethene, ethyne and benzene, most of which are common tracers of combustion activities (Liu et al., 2008). In view of the high mixing ratios of some halogenated hydrocarbons (HHs) including CH_3Cl, methyl iodine (CH_3I) and 1,2-

dichloroethane (1,2-DCE), we infer that VOCs in Case II were associated with coal and/or biomass burning. Besides, Case II air masses contained more abundant C_3-C_5 alkyl nitrates (ANs), which moderately correlated with these HHs, with the maximum correlation coefficient (r) ranging from 0.41 for 2-pentyl nitrate *vs.* 1,2-DCE to 0.89 for *i*-propyl nitrate *vs.* 1,2-DCE. Thus, combustion activities also accounted for the enrichments of C_3-C_5 ANs in Case II air masses. In fact, emissions of ANs from biomass burning have been confirmed in previous studies (Simpson et al., 2002; Lyu et al., 2017a). Most of VOC species showed the lowest mixing ratios in Case III air masses. In comparison with those in Case I, only methyl iodine (CH_3I) exhibited higher levels in Case III, likely resulting from marine emissions in SCS (Blake et al., 1999). A few alkanes (*i*-pentane and cyclopentane) and alkenes (propene, 1,3-butadiene and *cis*-2-butene) were more abundant in Case III than in Case II, which might be ascribed to vehicular and industrial emissions (Liu et al., 2008).

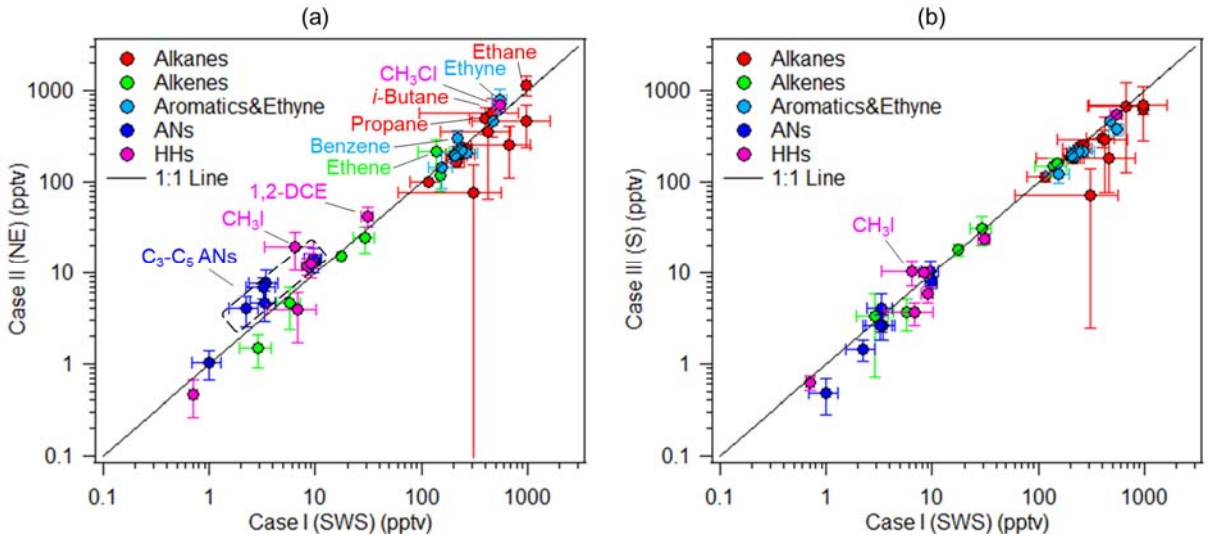

Figure 4. Scatter plots of average VOC mixing ratios in Case II (a) and Case III (b) against those of corresponding species in Case I. Error bars represent 95% C.I.s.

In conclusion, the old-growth forest significantly contributed to VOCs at SNJ, whereas the impacts of vehicular and industrial emissions from the southwest and south, and combustion emissions from the northeast were also obvious.

3.3. In-situ photochemistry

In this study, the purpose of applying the box model was not to simulate O_3, which was hardly achieved due to significant impacts of transport on O_3 in high-elevation and remote region. Instead, we aimed to assess the in-situ photochemistry, irrespective of origins of the air masses and how the air pollutants were transported to the site. The modelling results were acceptable under the premise that both O_3 and its precursors were reasonably constrained to observations (Figure S1).

Figure 5 shows the main reactions responsible for O_3 formation and budget balance of oxidative radicals. The reaction rates were calculated as averages over the period of 7:00–17:00. According to the simulations, the net ozone production rate (OPR) was 0.32 ± 0.06 ppbv hr^{-1}, comparable to

that at WLG on the Qinghai-Tibet Plateau (0.26–0.31 ppbv hr^{-1}) (Xue et al., 2013), but much lower than those at another mountainous site with the height of 750 m in central China (2.5–4.7 ppbv hr^{-1}) (Lei et al., 2021) and at Mt. Tai in the NCP (6.4 ppbv/hr) (Kanaya et al., 2009). The low OPR was in line with the trough in daytime section of the diurnal cycle of O_3. Alkyl peroxyl radicals (RO_2) reacting with NO (66.7%) outweighed the reaction between hydroperoxyl radical (HO_2) and NO (33.3%) in leading to O_3 production, while the destruction to O_3 was mainly comprised of ozonolysis of VOCs (60.9%), O_3 reacting with HO_2 (19.6%) and O_3 photolysis (17.4%). Reactions of OH + NO_2 (1.3%) and O_3 + OH (0.9%) played negligible roles in reducing O_3 production. This signified that O_3 photochemistry at this background site significantly differed from that in polluted atmosphere, where OH reacting with NO_2 and O_3 photolysis are generally the primary O_3 destruction pathways (Xue et al., 2016; Liu et al., 2019). During the period of 18:00–6:00, O_3 was chemically consumed at an average rate of -0.23 ± 0.03 ppbv hr^{-1}, which was exclusively dominated by ozonolysis of VOCs (92.2%).

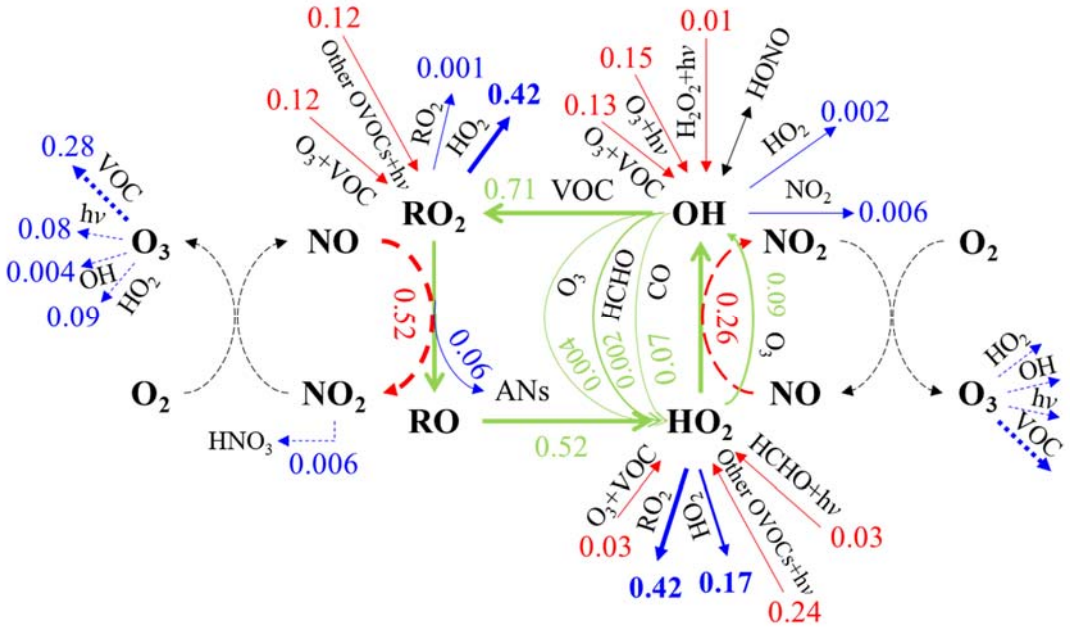

Figure 5. Main reactions responsible for O_3 formation (dashed lines with red and blue color denoting production and destruction pathways, respectively) and sources (solid red lines), sinks (solid blue lines) and cycling (solid green lines) of radicals. The numbers are average reaction rates over the period of 7:00–17:00 (ppbv hr^{-1}).

The modelled concentrations of RO_x radicals, including OH, HO_2 and RO_2, were at the low ends of the respective ranges of those simulated/measured in other high-elevation and/or forested regions (Table S5). An exception was that the RO_2 concentration (35.9 ± 1.9 pptv) was higher than that at WLG (18.9 pptv), in spite of the lower OH and HO_2, implying the less efficient transformation from RO_2 to HO_2 at SNJ. Besides, the ratio of HO_2/OH (635 pptv/pptv) at SNJ was notably higher than that simulated at WLG (83 pptv/pptv). The results were likely associated with the more abundant VOCs and low levels of NO_x at SNJ. We noticed that the HO_2/OH ratio at SNJ was on the same magnitude as those measured in some isoprene-rich and NO_x-lean environments,

e.g., 454 pptv/pptv in California Sierra Nevada Mountains (Mao et al., 2012). Fundamentally, this could be explained by the RO_x cycling, as shown in Figure 5. The cycling rate was 0.71 ppbv hr^{-1} for the transformation from OH to RO_2 (written as OH–RO_2, same for others). However, due to insufficient NO_x, it decreased to 0.52 ppbv hr^{-1} for RO_2–HO_2, and was further restricted to 0.26 ppbv hr^{-1} for HO_2–OH. The equilibrium for each radical was maintained via other pathways, especially the self-reactions as sinks. A large fraction (~42.0%) of RO_2 was consumed by reacting with HO_2 (0.42 ppbv hr^{-1}). Similarly, the reaction between HO_2 and RO_2 (HO_2) constituted 44.7% (18.1%) of the total loss rate of HO_2, and only 37.2% of HO_2 was converted to OH. Overall, the sinks of RO_x at SNJ were mainly through self-reactions of peroxyl radicals which are typical chain termination reactions in NO_x-lean environment (Thornton et al., 2002), in contrast to the reaction of OH + NO_2 in polluted atmosphere (Xue et al., 2016).

To further reveal the roles of O_3 precursors in modulating the in-situ photochemistry, sensitivity analysis was performed through increasing the model inputs by 10%. Since weather was highly changeable at the high-elevation site, the sensitivity to solar radiation was also tested. Table 2 summarizes the percentage changes in RO_x concentrations and rates of reactions involved in O_3 production and destruction, in response to the addition of 10% of O_3 precursors or 10% increase of solar radiations. The net OPR was most sensitive to NO, which increased by 22.9% with the addition of 10% of NO. The breakdowns of the net OPR clearly indicated the acceleration of the O_3 production pathways (HO_2 + NO, RO_2 + NO). While the rates of some O_3 destruction pathways (OH + O_3, HO_2 + O_3, OH + NO_2) were also enhanced, these reactions were much slower than the O_3 productions (Figure 5). Initiated with the accelerated reaction of RO_2 + NO, the RO_2 concentration decreased, in contrast to the rise of HO_2 and OH levels. The addition of CO facilitated transformation of OH to HO_2, which however restrained the production of RO_2, due to the consumption of OH and its low concentration in this reaction system. Restrictions on the two O_3 production pathways were still not alleviated, thereby minor impacts of the added CO on net OPR. This was also applicable to the additions of AVOC and BVOC. Moreover, the addition of VOCs speeded up the reactions of O_3 + VOC, the dominant O_3 destruction pathway at SNJ. As a result, the added VOCs made nil or even negative contributions to the net OPR. It is noteworthy that both CO and VOCs caused net consumptions of OH. Isoprene alone accounted for 33.4% of the total reaction rate of OH-initiated oxidations of VOCs, manifesting as the principal OH depleting species. The intensified solar radiation caused an increase of net OPR, with the sensitivity of 0.38 (3.8%/10%). The decrease of the reaction rate of OH + NO_2 was attributable to the enhanced photolysis of NO_2.

Overall, both O_3 formation and RO_x cycling were significantly limited by the insufficient NO_x at SNJ. CO and VOCs, especially isoprene, caused OH deficit, because the peroxyl radicals generated from the OH-initiated oxidations could not be efficiently returned to OH.

Table 2. Percentage changes in RO_x concentrations and reaction rates of pathways modulating net O_3 production in response to 10% increases of O_3 precursors or solar radiations (Unit: %).

Pathways / Radicals		NO	CO	AVOC*	BVOC#	S.R.
O_3 Production	HO_2 + NO	16.2	0.7	0.4	-1.3	1.9
	RO_2 + NO	8.9	-0.4	2.0	1.5	3.2

O_3 Destruction	$O^1D + H_2O$	-0.01	-0.04	0.01	-0.03	10.0
	$OH + O_3$	4.7	-0.5	-1.2	-3.5	3.0
	$HO_2 + O_3$	3.8	0.4	1.4	0.8	1.0
	$OH + NO_2$	16.7	-0.3	-1.1	-4.4	-4.8
	O_3 + VOC	-0.03	-0.02	4.1	5.9	-0.004
Net OPR		22.9	-0.3	0.1	-2.7	3.8
Oxidative Radicals	OH	4.6	-0.5	-1.2	-3.5	3.0
	HO_2	3.7	0.4	1.4	0.8	1.0
	RO_2	-3.0	-0.7	3.2	3.7	2.4

* and #: 65 and 3 VOC species are included in AVOC and BVOC, respectively. S.R.: Solar Radiation.

4. Conclusions

The observations of O_3 and its precursors in a high-elevation and highly forested region in central China, in combination with literature and public data, indicated that O_3 levels in the FT over China were higher than those over the United States and Europe. The O_3 concentrations were high enough to cause damages to the old-growth forest in the study region. Air masses from the north were characterized by elevated levels of O_3, which however did not show big differences from those in air masses of other origins. The adjacent southwest and south territories were significant source regions of NO, SO_2 and $PM_{2.5}$ at the site, but air from the northeast contained higher levels of CO. We identified abundant VOCs in this background atmosphere. In addition to local biogenic emissions, vehicular and industrial emissions in adjoining regions to the southwest and south, as well as combustion activities in regions to the northeast, were the potential sources of VOCs at the site. This study provides rare insights into the in-situ O_3 photochemistry in remote regions. It was revealed that O_3 production was significantly limited by the insufficient NO_x, which also caused intensive self-reactions among RO_x radicals. The in-situ O_3 production was not sensitive to CO and AVOCs, while BVOCs even made some negative contributions to the net O_3 production rate. Both CO and VOCs caused net consumptions of OH, and the first position of OH depleting species was occupied by isoprene. Therefore, it was most likely that the old-growth forest did not aggravate O_3 injuries to itself by releasing VOCs. The in-situ modelling could not rule out the possibility of CO and VOCs fueling O_3 formation during the transport of them to the site. This study highlighted high levels of FT O_3 over China, and provided evidence of regional transport affecting air quality in central China. The observational data in such a region without any high-elevation or ozonesonde measurements before will provide important references for future studies.

Acknowledgements

This study was supported by the Research Grants Council of the Hong Kong Special Administrative Region via Theme-Based Research Scheme (TRS) (Project T24-504/17-N), and the Strategic Focus Area scheme of The Research Institute for Sustainable Urban Development at

The Hong Kong Polytechnic University (1-BBW9). The observation data are available in an online data repository (Lyu, 2020).

References

Atkinson, R. (2000). Atmospheric chemistry of VOCs and NO_x. *Atmospheric Environment, 34*(12-14), 2063–2101.

Atkinson, R. & Aschmann, S.M. (1993). Hydroxyl radical production from the gas-phase reactions of ozone with a series of alkenes under atmospheric conditions. *Environmental Science & Technology, 27*(7), 1357–1363.

Blake, N.J., Blake, D.R., Wingenter, O.W., Sive, B.C., Kang, C.H., Thornton, D.C., et al. (1999). Aircraft measurements of the latitudinal, vertical, and seasonal variations of NMHCs, methyl nitrate, methyl halides, and DMS during the First Aerosol Characterization Experiment (ACE 1). *Journal of Geophysical Research: Atmospheres*. *104*(D17), 21803–21817.

Cui, J., Pandey Deolal, S., Sprenger, M., Henne, S., Staehelin, J., Steinbacher, M. & Nédélec, P. (2011). Free tropospheric ozone changes over Europe as observed at Jungfraujoch (1990–2008): An analysis based on backward trajectories. *Journal of Geophysical Research: Atmospheres*, 116, D10304. https://doi.org/10.1029/2010JD015154.

Dunlea, E.J., Herndon, S.C., Nelson, D.D., Volkamer, R.M., San Martini, F., Sheehy, P.M., et al. (2007). Evaluation of nitrogen dioxide chemiluminescence monitors in a polluted urban environment. *Atmospheric Chemistry & Physics, 7*, 2691–2704.

Fishman, J., Ramanathan, V., Crutzen, P.J. & Liu, S.C. (1979). Tropospheric ozone and climate. *Nature, 282*(5741), 818–820.

Geernaert, G. & Zlatev, Z. (2004). Studying the influence of biogenic emissions on AOT40 levels in Europe. *International Journal of Environment and Pollution*, 22(1-2), 29–42.

Hocking, W.K., Carey-Smith, T., Tarasick, D.W., Argall, P.S., Strong, K., Rochon, Y., et al. (2007). Detection of stratospheric ozone intrusions by windprofiler radars. *Nature, 450*(7167), 281–284.

Hegglin, M.I., Fahey, D.W., McFarland, M., Montzka, S.A. & Nash, E.R. (2015). Twenty questions and answers about the ozone layer: 2014 Update-Scientific Assessment of Ozone Depletion: 2014. Geneva, Switzerland: World Meteorological Organization.

Kanaya, Y., Pochanart, P., Liu, Y., Li, J., Tanimoto, H., Kato, S., et al. (2009). Rates and regimes of photochemical ozone production over Central East China in June 2006: a box model analysis using comprehensive measurements of ozone precursors. *Atmospheric Chemistry & Physics, 9*(20), 7711–7723.

Lippmann, M. (1991). Health effects of tropospheric ozone. *Environmental Science & Technology*, *25*(12), 1954–1962.

Lei, X., Cheng, H., Peng, J., Jiang, H., Lyu, X., Zeng, P., et al. (2021). Impact of long-range atmospheric transport on volatile organic compounds and ozone photochemistry at a regional background site in central China. *Atmospheric Environment*, *246*, doi.org/10.1016/j.atmosenv.2020.118093.

Lyu, X. (2020). Observation data at Shennongjia - Criteria air pollutants, VOCs, OVOCs, and meteorological parameters. figshare. Dataset. https://doi.org/10.6084/m9.figshare.12950528.v1.

Lu, X., Chen, N., Wang, Y., Cao, W., Zhu, B., Yao, T., et al. (2017). Radical budget and ozone chemistry during autumn in the atmosphere of an urban site in central China. *Journal of Geophysical Research: Atmospheres, 122*(6), 3672–3685.

Lyu, X.P., Guo, H., Wang, N., Simpson, I.J., Cheng, H.R., Zeng, L.W., et al. (2017a). Modeling C_1–C_4 alkyl nitrate photochemistry and their impacts on O_3 production in urban and suburban environments of Hong Kong. *Journal of Geophysical Research: Atmospheres. 122*(19), 10539–10556.

Lin, M., Horowitz, L.W., Oltmans, S.J., Fiore, A.M. & Fan, S. (2014). Tropospheric ozone trends at Mauna Loa Observatory tied to decadal climate variability. *Nature Geoscience, 7*(2), 136–143.

Li, K., Jacob, D.J., Liao, H., Shen, L., Zhang, Q. & Bates, K.H. (2019a). Anthropogenic drivers of 2013-2017 trends in summer surface ozone in China. *Proceedings of the National Academy of Sciences, 116*(2), 422–427.

Liu, X., Lyu, X., Wang, Y., Jiang, F. & Guo, H. (2019). Intercomparison of O_3 formation and radical chemistry in the past decade at a suburban site in Hong Kong. *Atmospheric Chemistry & Physics, 19*, 5127–5145.

Liu, Y., Shao, M., Fu, L., Lu, S., Zeng, L. & Tang, D. (2008). Source profiles of volatile organic compounds (VOCs) measured in China: Part I. *Atmospheric Environment, 42*(25), 6247–6260.

Logan, J.A., Staehelin, J., Megretskaia, I.A., Cammas, J.P., Thouret, V., Claude, H., et al. (2012). Changes in ozone over Europe: Analysis of ozone measurements from sondes, regular aircraft (MOZAIC) and alpine surface sites. *Journal of Geophysical Research: Atmospheres*. 117, D09301, https://doi.org/10.1029/2011JD016952.

Liu, Y. & Wang, T. (2020). Worsening urban ozone pollution in China from 2013 to 2017-Part 2: The effects of emission changes and implications for multi-pollutant control. Atmospheric Chemistry and Physics. 20(11):6323-6337.

Lyu, X.P., Wang, N., Guo, H., Xue, L.K., Jiang, F., Zeren, Y.Z., et al. (2019). Causes of a continuous summertime O_3 pollution event in Jinan, a central city in the North China Plain. *Atmospheric Chemistry & Physics, 19*, 3025–3042.

Lyu, X.P., Zeng, L.W., Guo, H., Simpson, I.J., Ling, Z.H., Wang, Y., et al. (2017b). Evaluation of the effectiveness of air pollution control measures in Hong Kong. *Environmental Pollution, 220*, 87–94.

Mao, J., Ren, X., Zhang, L., Van Duin, D.M., Cohen, R.C., Park, J.H., et al. (2012). Insights into hydroxyl measurements and atmospheric oxidation in a California forest. *Atmospheric Chemistry & Physics, 12*, 8009–8020.

Reich, P.B. & Amundson, R.G. (1985). Ambient levels of ozone reduce net photosynthesis in tree and crop species. *Science, 230*(4725), 566–570.

Sun, L., Xue, L., Wang, T., Gao, J., Ding, A., Cooper, O.R., et al. (2016). Significant increase of summertime ozone at Mount Tai in Central Eastern China. *Atmospheric Chemistry & Physics, 16*, 10637–10650.

Thornton, J.A., Wooldridge, P.J., Cohen, R.C., Martinez, M., Harder, H., Brune, W.H., et al. (2002). Ozone production rates as a function of NOx abundances and HOx production rates in the Nashville urban plume. *Journal of Geophysical Research: Atmospheres*, *107*(D12), doi.org/10.1029/2001JD000932.

Wang, Y., Wang, H., Guo, H., Lyu, X., Cheng, H., Ling, Z., et al. (2017). Long-term O_3–precursor relationships in Hong Kong: field observation and model simulation. *Atmospheric Chemistry & Physics. 17*(18), 10919–10935.

Xue, L., Gu, R., Wang, T., Wang, X., Saunders, S., Blake, D., et al. (2016). Oxidative capacity and radical chemistry in the polluted atmosphere of Hong Kong and Pearl River Delta region: analysis of a severe photochemical smog episode. *Atmospheric Chemistry and Physics*, *16*(15), 9891-9903.

Xu, W., Lin, W., Xu, X., Tang, J., Huang, J., Wu, H. & Zhang, X. (2016). Long-term trends of surface ozone and its influencing factors at the Mt Waliguan GAW station, China–Part 1: Overall trends and characteristics. *Atmospheric Chemistry & Physics, 16*(10), 6191–6205.

Xue, L.K., Wang, T., Guo, H., Blake, D.R., Tang, J., Zhang, X.C., et al. (2013). Sources and photochemistry of volatile organic compounds in the remote atmosphere of western China: results from the Mt. Waliguan Observatory. *Atmospheric Chemistry & Physics, 13*(17), 8551–8567.

Xu, Z., Wang, T., Xue, L.K., Louie, P.K., Luk, C.W., Gao, J., et al. (2013). Evaluating the uncertainties of thermal catalytic conversion in measuring atmospheric nitrogen dioxide at four differently polluted sites in China. *Atmospheric Environment, 76*, 221–226.

Xue, L.K., Wang, T., Zhang, J.M., Zhang, X.C., Poon, C.N., Ding, A.J., et al. (2011). Source of surface ozone and reactive nitrogen speciation at Mount Waliguan in western China: new insights from the 2006 summer study. *Journal of Geophysical Research: Atmospheres*, 116, D07306, https://doi.org/10.1029/2010JD014735.

Xu, W.Y., Xu, X.B., Lin, M.Y., Lin, W.L., Tarasick, D., Tang, J., et al. (2018). Long-term trends of surface ozone and its influencing factors at the Mt Waliguan GAW station, China-Part 2: the roles of anthropogenic emissions and climate variability. *Atmospheric Chemistry & Physics, 18*, 773–798.

Zeng, P., Lyu, X.P., Guo, H., Cheng, H.R., Jiang, F., Pan, W.Z., et al. (2018). Causes of ozone pollution in summer in Wuhan, Central China. *Environmental Pollution. 241*, 852–861.

Zhu, Y., Yang, L., Kawamura, K., Chen, J., Ono, K., Wang, X., et al. (2017). Contributions and source identification of biogenic and anthropogenic hydrocarbons to secondary organic aerosols at Mt. Tai in 2014. *Environmental Pollution, 220*, 863–872.